# Chapter 9

# X-ray Phase Contrast: Research on a Future Imaging Modality

Authors: Johannes Bopp, Lina Felsner, Shiyang Hu, Sebastian Kaeppler, and Christian Riess



## 9.1 Introduction

Modern medical imaging is achieved with state-of-the-art devices, that use cutting-edge technology from different fields of engineering. Oftentimes, progress is driven by discoveries in a at first sight seemingly unrelated field of research. This enables the construction of new devices that was thought to be impossible before. In this chapter, we introduce a new imaging modality that has the potential to develop into a future medical imaging technology: X-ray phase-contrast imaging. At its current state, its medical use still has to be demonstrated. Yet, several early experimental results indicate that it has some potential for clinical applications.

Conventional X-ray imaging measures the attenuation of X-rays. X-ray attenuation happens due to different interactions between X-ray photons


A. Maier et al. (Eds.): Medical Imaging Systems, LNCS 11111, pp. 191–205, 2018.
https://doi.org/10.1007/978-3-319-96520-8_9

**Geek Box 9.1: Complex Index of Refraction**

As stated in Chapter 5, light propagation can be modeled with the index of refraction $n$. When operating at X-ray energies, the index of refraction is expressed as a complex number,

$$n_{\text{complex}} = 1 - \delta + \mathrm{i}\beta \ , \tag{9.1}$$

where the imaginary coefficient $\beta$ models attenuation and the real coefficient $\delta$ models phase shift. At X-ray energies, $n_{\text{complex}}$ is very close to 1, i. e., little attenuation and refraction occurs. For example, for a transition between vacuum and water at a (relatively low) X-ray energy of 20 keV, $\beta = 3.99411 \cdot 10^{-10}$ and $\delta = 5.76149 \cdot 10^{-07}$. Note that for this configuration, $\delta$ is by about a factor 1000 larger than $\beta$. If we loosely identify $\beta$ with the quantity measured in traditional X-ray, and $\delta$ with the quantity measured in phase-sensitive X-ray, we get an intuition about the vision of early attempts to translate phase-sensitive X-ray into the hospital: shouldn't it be possible with phase-sensitive X-ray systems to obtain a signal that is 1000 times stronger at a radiation dose equal to traditional X-ray? Later research has shown that the necessary compromises in system design to measure phase consume most of this advantage.

and matter (see Chapter 7 for details). However, attenuation does not fully describe X-ray interaction with matter. In the early 1930s, phase contrast microscopy, described in Chapter 5, was introduced. It measures refraction of visible light, which provides an alternative to standard transmission microscopy for mostly translucent objects, such as biological cells. Since visible light and X-ray are both electromagnetic waves, it is theoretically possible to transfer this principle to X-ray imaging. To measure X-ray refraction has two motivations: First, it may allow visualizing materials whose attenuation properties differ only slightly. Second, it was assumed that refraction information would deliver improved contrast over attenuation (see Geek Box 9.1 for details).

However, since the wavelength of X-rays is several orders of magnitude smaller than the wavelength of visible light, it took several decades until manufacturing technologies were developed to realize X-ray phase-contrast imaging.

Several systems have been designed for phase contrast imaging. While all of these approaches are highly interesting from a physics point of view, we limit the presentation in this chapter to the Talbot-Lau Interferometer (TLI). A short description of other approaches can be found in the Geek Box 9.2. Most of these other approaches are more sensitive than TLI, but TLI's relative

**Geek Box 9.2: Other Setups**

A number of different systems have been proposed to measure the phase of light at X-ray energies. Below is a list of setups that have been regularly mentioned in the recent literature.

- **Propagation-based:** This is probably the simplest phase-sensitive design. Phase is measured via interference: a wavefront that is refracted by a material interferes with itself [19, 22]. To compute the refraction (and hence the phase), it suffices to acquire two or more traditional X-ray images with varying detector distance. On the downside, interference only occurs if the X-ray source has a very small focal spot and the distance between object and detector is large enough. X-ray tubes with a small focal spot currently suffer from low flux, which limits practical applications.
- **Edge illumination:** This setup aims at directly measuring refraction by placing absorption masks in the beam path [14]. Depending on how much the object refracts the beam, a larger or smaller part of a detector pixel is illuminated. This design is conceptually very straightforward, but due to the direct measurement of the angle of refraction, it is less sensitive than other systems.
- **Analyzer-based:** Analyzer-based systems operate on monochromatic X-rays, which allows to precisely measure the refractive angle for a material [6, 4]. The beam is reflected by a crystal (the so-called "analyzer") behind the object. This crystal has the special property that it reflects radiation only at the Bragg angle, i. e., in a very narrow angular interval. Rocking the crystal allows to precisely measure all occurring angles of refraction. While this setup is extremely sensitive to mechanical motion and requires monochromatic X-rays, it is unmatched in its sensitivity and dose efficiency.
- **Speckle tracking:** Another approach to direct phase measurement is to track the refraction of a predefined pattern in the beam path [3]. One can obtain such a pattern by introducing for example a sheet of sandpaper in the beam path. Speckle tracking works best on thin samples and also requires an X-ray source with a small focal spot.

mild system requirements make it currently the most attractive system for implementation in a clinical setup. In particular, it only requires additional gratings to be mounted between a regular medical X-ray tube and detector to be operated. Note that all of the methods presented in this chapter are current research topics and none of them are clinically used at present. However, it is expected that the presented methods will have clinical impact in the future.

We introduce some physical preliminaries, and then the Talbot-Lau interferometer itself. As an outlook, we present potential applications of this modality in medicine and visual inspection.

## 9.2 Talbot-Lau Interferometer

One of the most promising phase-sensitive setups for medical applications is the so-called Talbot-Lau interferometer (TLI) [5, 15]. It roots in Young's famous double-slit experiment from 1801 to demonstrate interference. Young performed the experiment with visible light, but it can be directly adapted to X-ray. A sketch of this experiment is shown in Fig. 9.1 (left). The light source, in our case an X-ray source, is shown on the left. We assume that X-rays only emerge from a small source point, indicated by the narrow slit on the left. There is a barrier with two narrow slits in the beam path at some distance before an X-ray detector. The observation of the double-slit experiment is that an interference pattern shows at the detector, that is a regular pattern of bright and dark spots. The origin of the interference pattern is illustrated in Fig. 9.1 (right). The interference pattern is determined by the path difference $\Delta d$ of the two traveling X-ray waves from both slits, namely

$$\Delta d = d \sin(\theta) \ , \tag{9.2}$$

where $d$ is the distance between the two origins. Here, we assume that the distance $D$ between the slits and the screen is large, such that $\vartheta$ is close to zero and $\theta \approx \vartheta$. Constructive interference shows as a bright spot. It occurs when the waves arrive "in phase". This is the case if the path difference is zero or an integral multiple of the wavelength,

$$\Delta d = d \sin(\theta) = m\lambda \ , \quad m \in \mathbb{Z} \ . \tag{9.3}$$

Destructive interference appears as a dark spot. It occurs if the path length differs by half the wave length,

$$\Delta d = d \sin(\theta) = (m + \frac{1}{2})\lambda \ , \quad m \in \mathbb{Z} \ . \tag{9.4}$$

Gray spots are observed if the difference of path length is between these two cases.

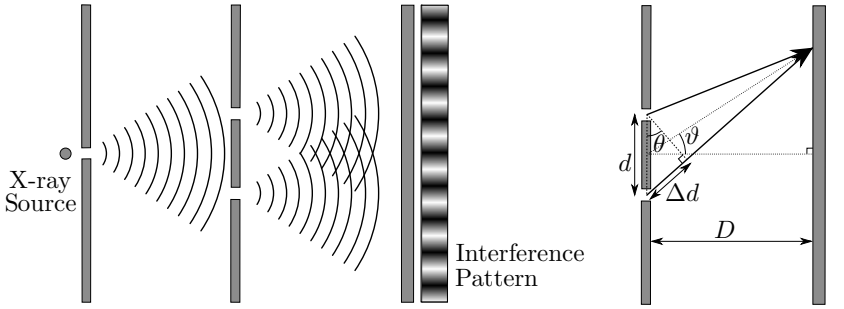


**Figure 9.1:** Young's Double-Slit Experiment

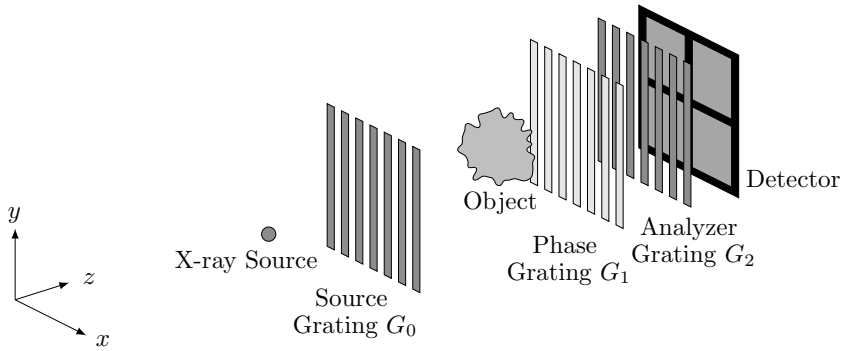


**Figure 9.2:** Talbot-Lau interferometer. Between X-ray source and detector, the three gratings $G_0$, $G_1$, $G_2$ form an interferometer.

### 9.2.1 Talbot-Lau Interferometer Setup

The Talbot-Lau interferometer makes use of the interference effect. It consists of a conventional X-ray device with three rectangular gratings $G_0$, $G_1$, and $G_2$ in the beam line (Fig. 9.2). These gratings typically have a period between 1 and 20 µm and a duty cycle of 0.5, i. e., grating bars and slits have the same width. $G_1$ is a phase grating and constitutes the core of the interferometer. $G_0$ and $G_2$ have supporting functions and will be introduced later.

At slits of grating $G_1$, the wave passes without notable modification. At bars of grating $G_1$, the phase of the incoming wave is shifted by an additive factor between 0 and $2\pi$. This is a trick to construct from Young's double-slit experiment an actual imaging system. Constructive or destructive interference can now happen between wave sections traveling through two grating slits (as stated above), or between wave sections traveling through a grating slit and a grating bar. In the second case, the path difference $\Delta d$ between a

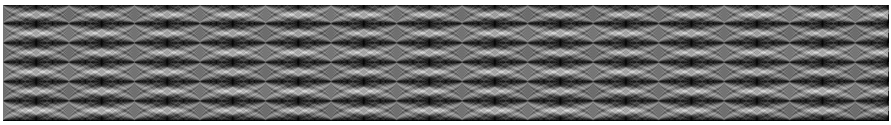

**Figure 9.3:** Simulated Talbot carpet: interference pattern behind grating $G_1$ travelling from left to right.

grating bar and a grating slit must now add up to the imprinted phase shift for constructive interference. Due to the Talbot effect, these interference patterns cleanly overlay at the so-called Talbot distances. Fig. 9.3 shows a simulation of the interference pattern behind grating $G_1$. The wave is assumed to travel from left to right. The detector is placed at a location where constructive and destructive interference form a clearly distinguishable black-and-white pattern. However, the pattern periodically repeats, which is why a system designer can in theory choose from infinitely many positions to place the detector. In practice, however, the pattern quickly washes out, such that the detector has to be located at one of the first replications of the pattern.

Gratings $G_0$ and $G_2$ are used to solve several engineering problems such that the interferometer can be built within compact medical X-ray setups. The interference pattern at the detector is normally much smaller than a single detector pixel. To resolve the pattern, the analyzer grating $G_2$ is used. $G_2$ is an absorption grating such that only a part of the interference pattern passes through the slits onto the detector. This makes it possible to sample the interference pattern by taking X-ray images while moving $G_2$ along the pattern (which is further discussed in Sec. 9.2.2).

Grating $G_0$ addresses another practical problem, namely the size of the focal spot. Interference effects can only be observed on coherent waves. In the sketch on Young's double-slit experiment in Fig. 9.1, coherence is obtained automatically by the small slit behind the X-ray source, which effectively acts as a small focal spot. There exist so-called microfocus X-ray sources that do provide such a small focal spot but they produce only very few X-rays per time. For practical applications, the imaging times are typically much too long. Medical X-ray tubes produce orders of magnitude more X-rays, which allows to take an X-ray image within a fraction of a second. However, such X-ray tubes can only be built with a focal spot that is much larger, typically between half a millimeter and a millimeter. To overcome this issue, grating $G_0$ is used, which can be seen as a long array of micrometer-sized slits. Each slit acts as a microfocus spot and creates an interference pattern at the detector. The distances between the slits are now chosen in a way that the pattern of each of the slits exactly overlays with the pattern of the other slits. If the setup parameters are chosen correctly (cf. Geek Box 9.3), all these periodic structures at the detector are aligned and add up. This enables imaging using conventional X-ray sources.

**Geek Box 9.3: Talbot-Lau Setup Parameters**

As described in Section 9.2 the TLI consists of three gratings, a medical X-ray source, and a detector. Many details on the construction of a Talbot-Lau interferometer can be found for example in the Ph.D. thesis by Martin Bech [2].
Optimization of the imaging performance of the whole setup requires to explore a huge parameter space. Each grating design already has multiple degrees of freedom. First of all, the grating material has to be chosen. Typical materials are gold, nickel and aluminum. The choice of the material and the manufacturing technology can constrain the other parameters of the grating, such as the height, period and duty cycle. The duty cycle is the ratio between the width of a grating bar and one grating period. Typical grating periods lie in the rage between 1 µm and 10 µm. Additionally, the grating aspect ratio, which is the grating height divided by the width, is currently limited to about 50.
The design of one grating can not be done in isolation. Instead, the whole imaging system has to be considered. For example, The Talbot effect yields a limited set of possible distances between $G_1$ and $G_2$ for a specific energy. Another example is the $G_0$ grating, where the Lau effect can be used to fix either its period or its position.
Due to the huge parameter space, parameters dependencies and the polychromatic spectrum of medical X-ray tubes, optimization of a setup is challenging. In practice, one tries to hold most of the parameters fix. Then, the remaining parameters space is explored by simulating the corresponding interferometer using numerical wave front propagation algorithms.

One quality measure of the TLI can be derived from the system setup directly, the so-called sensitivity $s$,

$$s = \frac{\mathrm{dist}(\mathrm{G}_1, \mathrm{G}_2)}{2\pi p_2} \quad , \tag{9.5}$$

defined by the distance between $G_1$ and $G_2$ and $p_2$ which is the period of the analyzer grating $G_2$. The sensitivity can be interpreted as an "amplification factor" of the refractive angle.

### 9.2.2 Phase Stepping and Reconstruction

Phase stepping denotes the process of shifting one of the gratings (typically $G_2$) by a fraction of its period to sample the interference pattern. This is

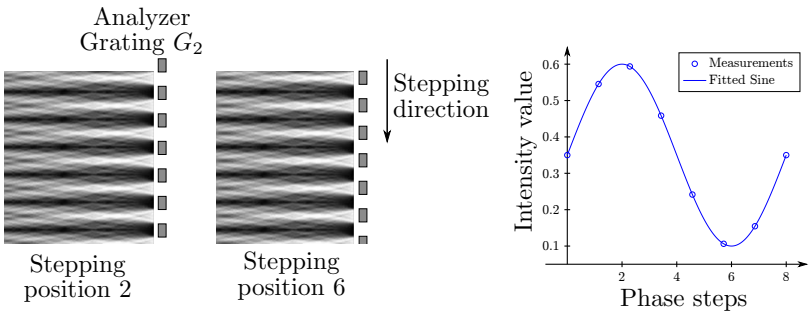


**Figure 9.4:** Left: phase stepping. The Talbot carpet is sampled at different positions of grating $G_2$. Right: the intensities at different stepping positions form the sinusoidal phase stepping curve. From this curve, attenuation, differential phase and dark-field can be calculated.

shown in Fig. 9.4 (left): the Talbot carpet forms the interference pattern. At equidistant stepping positions, the detector records an image. The intensity values for a pixel at different stepping positions is called phase stepping curve. This curve can be considered as a convolution of the profile of $G_2$ with the intensity pattern of the $G_1$ pattern. Convolution of two rectangular functions of $G_1$ and $G_2$ leads ideally to a triangular signal. In reality, blurring from the slits of $G_0$ leads to a sinusoidal curve that is fitted to the measured steps. These steps are shown in Fig. 9.4 (right). After fitting a sine function to the phase stepping curve, three quantities can be calculated: attenuation, differential phase, and dark-field. Attenuation is the offset of the intensities, which can be computed as the average of all intensities of the phase stepping curve. Differential phase is the phase offset of the sine. Dark-field is one minus the ratio between amplitude of the curve and two times attenuation.

In practice, these three quantities cannot be calculated directly. Instead, it is necessary to acquire two scans: a reference scan and an object scan. The reference scan is acquired without an object in the beam path such that it only shows the background. It captures inhomogeneities in the setup, for example, in the grating bars. The object scan is acquired with an object before or behind $G_1$. The reference scan is used to normalize the object scan after calculating attenuation, differential phase, and dark-field for both scans. Several works address the further suppression of imaging artifacts in software [9, 8, 11]. More details on the calculation of attenuation, phase, and dark-field can be found in Geek Box 9.4.

A common metric for the quality of an interferometer is visibility. Visibility is a measure of contrast of the intensity modulation and is given by the sine amplitude divided by its offset. Thus, the dark-field signal corresponds to the reduction in interferometer visibility, for example, due to micro scattering.

**Geek Box 9.4: Signal Reconstruction**

Let us formalize the computation of attenuation, differential phase shift, and dark field information for each pixel. Let $R$ denote the wave profile of the reference scan and $O$ the wave profile of the object scan consisting each of $n$ phase steps. The calculation is performed for each pixel individually which is why we omit the pixel coordinate in the equations below. Attenuation is obtained as the average reference signal over the average object signal by computing

$$\mu = -\ln \left( \frac{\sum_{i=1}^{n} R_i}{\sum_{i=1}^{n} O_i} \right) .$$

The computation of the differential phase shift requires to find parameters for the sinusoidal phase stepping curve. The most robust way to do this is to perform least-squares curve fitting, which gives offset and amplitude of the sine. For the computation of the differential phase, the phase of object and reference wave profiles are subtracted.
The dark-field information $\xi$ is a function of the visibilities of the reference scan $V_R$ and the object scans $V_O$. $V_R$ is computed as

$$V_R = \frac{\max(R) - \min(R)}{\max(R) + \min(R)} ,$$

where the maximum and minimum operators refer to the maximum and minimum function values of the fitted sine curve on $R$. The visibility $V_O$ is computed in the same line. Then, the dark-field is defined as

$$D = -\ln \frac{V_R}{V_O} .$$

The visibility of the reference signal is considered an important figure of merit of the interferometer as it determines the noise in the differential phase and dark-field images.

## 9.3 Applications

An example for the three resulting signals is shown is Fig. 9.5. The shown gummi bears are modified with artificial defects, namely powder, a needle,

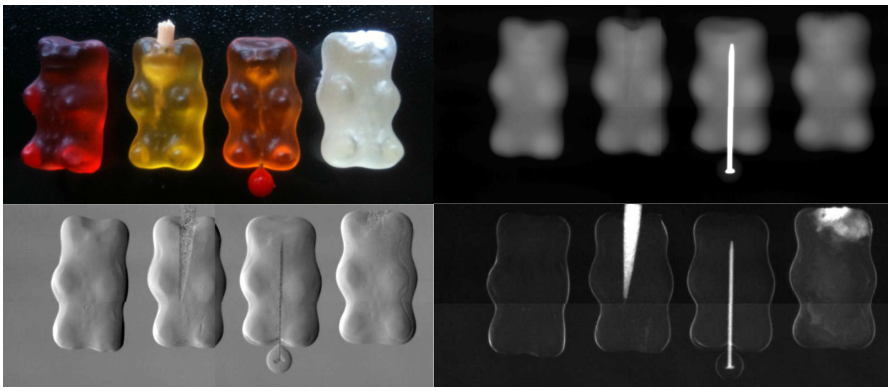

**Figure 9.5:** Top left: photograph of gummi bears with artificial defects. Attenuation (top right), differential phase (bottom left) and dark-field (bottom right) visualize different modifications in the gummi bears. Differential phase is particularly sensitive to high-frequency variations in the signal. Dark-field is particularly sensitive to micrometer-sized structural variations, such as powders or fibers. Pictures courtesy of ECAP Erlangen.

and a toothpick. In the top right, the absorption image is shown, which clearly shows the metal needle. On the bottom left, the differential phase is shown, which shows a large amount of high-frequency details, including the center of the needle head and the powder structure. In the bottom right, the dark-field signal is shown, which is particularly sensitive to the fine-grained structural variations in the powder and the toothpick.

An example scan on biological data is shown in Fig. 9.6. From left to right, the images show attenuation, differential phase, and dark-field of a female breast [10]. Particularly interesting in this visualization is the dark-field image, which is particularly sensitive to microcalicifications in the breast, a common indication for breast cancer.

Overall, X-ray attenuation visualizes both variations in density and atomic number. Thus, for example, it excels at the visualization of bones. Bones are more dense than the surrounding tissue and also contain a substantial amount of calcium.

Phase information on the other hand is sensitive to variations in electron density. Thus, it is expected to deliver increased contrast over attenuation when there is a similar elemental composition between two structures. One example is imaging of soft tissues. Talbot-Lau interferometers can only obtain differential phase information. Hence, its main advantage is in imaging high frequency details, such as edges that lie perpendicular to the grating bars. Conversely, it is less effective for imaging low-frequencies information.

Dark-field imaging provides two interesting properties that set it apart from absorption and differential phase: First, dark-field is sensitive to den-

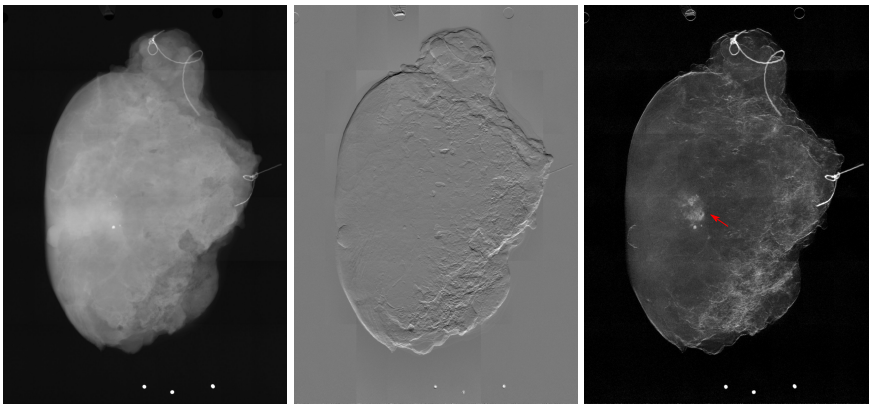

**Figure 9.6:** Attenuation, differential phase, and dark-field images of a female breast [10]. Microcalcifications in the dark-field signal (red arrows) can indicate cancer.

sity variation at nano- and micrometer scale. This is typically below the resolution of the detector, and as such too small to be resolved in attenuation imaging. Second, when scanning ordered structures such as fibers, the dark-field intensity varies with the angle between the fibers and the gratings. Both properties together can be used to deduce the orientation of fibers below the resolution limit of the detector [7, 12, 1]: when performing tomography on a plane in which micrometer-scaled fibers are located, the dark-field signal oscillates. From this oscillation, the direction of the fibers can be deduced, although the individual fibers are too small to be resolved by the detector. An example is shown in Fig. 9.7. On the left, a wooden block with different layers of wooden fibers is shown. This block is scanned in a tomographic setup, and the fiber orientations are deduced from the signal oscillations [1]. On the right of Fig. 9.7, the reconstructed orientations are shown, in different colors per layer.

Overall, phase-contrast and dark-field signals offer several interesting properties. It depends on the imaging task to decide whether the offerings of phase and dark-field signals or conventional attenuation is advantageous. The list below enumerates applications where Talbot-Lau imaging can potentially offer an advantage over traditional absorption imaging.

- **Mammography.** Mammography relies on imaging soft tissue structures in the breast, as well as on the detection of micro-calcifications. Imaging of soft tissues could benefit from the phase signal since it provides a strong signal to noise ratio at high frequencies. It has also been shown that the dark-field signal can reveal micro-calcifications that are invisible in the attenuation image since their porous structure creates dark-field signals [13].

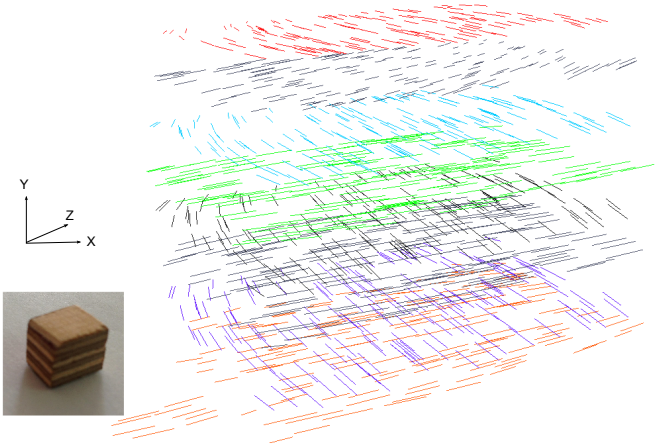


**Figure 9.7:** Layered wooden block (left) and example dark-field reconstruction of the dominant fiber orientations in each layer (right).

- **Lung imaging.** The human lung relies on millions of small alveoli to perform gas exchange. Lung diseases such as chronic obstructive pulmonary disease (COPD) and pulmonary fibrosis lead to a change in the structure of the alveoli. However, due to their small size, they cannot be resolved individually. The dark-field signal is able to detect abnormalities in the alveoli microstructure and may thus provide a benefit when diagnosing these diseases [23].
- **Bone imaging.** The directionality of the dark-field signal can possibly be used to detect osteoporosis, which can lead to less aligned structures in the bone [21]. Furthermore, the phase signal can visualize low contrast structures such as cartilage and tendons which may not be visible in attenuation imaging.
- **Micro-CT.** CT scanners which provide high resolutions (voxel sizes in the size of micrometers) are called Micro-CT systems. They are used for analyzing small samples and animals. At high resolutions, phase-contrast CT delivers a higher image quality than conventional CT [16]. This can be explained by the fact that the recorded phase signal is differential. A first Talbot-Lau Micro-CT system is commercially available [20].
- **Industrial applications.** Beyond medical imaging, dark-field imaging has been applied to non-destructive testing [18, 17]. For example, it can detect defects in carbon fibers or foreign bodies in food that are undetectable using attenuation imaging.

## 9.4 Research Challenges

The Talbot-Lau X-ray interferometer is an emerging image modality. Several questions need to be addressed before it can be applied in a clinical environment. Most notable issues are:

- **Grating manufacturing and mechanical setup.** Manufacturing grating structures with a period of a few micrometers and a sufficient grating height (in order to block high energy X-rays) is challenging. Thus, with current technology, the efficiency of the Talbot-Lau interferometer decreases with increasing photon energy. Additionally, the diameter of the gratings is limited to a few centimeters. Stitching procedures, which combine smaller gratings into a big grating, as well as smart scanning approaches that are compatible with smaller gratings are currently under research. Due to the small grating period, system stability in the nanometer range is required during operation. This stability is difficult to achieve in clinical environments.
- **Medical applications and dose.** A Talbot-Lau system is approximately half as dose-effective as a conventional X-ray system since the $G_2$ grating ideally absorbs half of the radiation. This leads to the question whether the additional information provided by a Talbot-Lau system is worth a reduction in attenuation dose efficiency. Economical aspects also need to be considered: manufacturing the gratings and their support structures adds considerable costs to an X-ray system. Is the benefit of the information provided by the Talbot-Lau system worth this cost?
- **Optimal system design.** Each grating introduces a new set of parameters into the system design (see Geek Box 9.3). Furthermore, the system does not only have to be optimized for attenuation, but also for phase and dark-field imaging performance. Due to this complexity, determining the optimal setup parameters (under the constraints provided by e. g., manufacturing) for a specific imaging task is still an open problem.
- **Image processing algorithms.** Image processing algorithms are needed in many steps of the conventional X-ray imaging pipeline, for example, for artifact correction, denoising, and visualization. Talbot-Lau interferometers suffer from additional issues (e. g. artifacts due to non-exact grating alignment). Also the differential phase and dark-field are affected by similar artifacts as the attenuation image, such as beam hardening. Additionally, the information retrieval from phase stepping data itself requires a reconstruction algorithm. Thus, image processing can be considered as a necessary component of a Talbot-Lau imaging system.
- **Tomographic reconstruction.** The phase information obtained by a Talbot-Lau interferometer can be reconstructed in a similar way to attenuation information by using an appropriate reconstruction filter, the so-called Hilbert filter. However, the dark-field signal (which contains scattering information) is directional and also influenced by signals at the object

edges. This makes its tomographic reconstruction challenging and has led to the development of dedicated algorithms to solve this problem [1].

## Further Readings

[1] F. L. Bayer et al. “Reconstruction of scalar and vectorial components in X-ray dark-field tomography”. In: *Proceedings of the National Academy of Sciences of the United States of America* 111.35 (Sept. 2014), pp. 12699–12704.

[2] M. Bech. “X-Ray Imaging with a Grating Interferometer”. PhD thesis. University of Copenhagen, 2009.

[3] S. Bérujon et al. “Two-Dimensional X-Ray Beam Phase Sensing”. In: *Physics Review Letter* 108 (2012), p. 158102.

[4] L. D. Chapman et al. “Diffraction Enhanced X-ray Imaging”. In: *Physics in Medicine and Biology* 42.11 (Nov. 1997), pp. 2015–2025.

[5] J. Clauser and M. Reinsch. “New theoretical and experimental results in Fresnel optics with applications to matter-wave and X-ray interferometry”. In: *Applied Physics B* 54.5 (1992), pp. 380–395.

[6] T. J. Davis et al. “Phase-contrast Imaging of Weakly Absorbing Materials using Hard X-rays”. In: *Nature* 373.6515 (Feb. 1995), pp. 595–598.

[7] T. H. Jensen et al. “Directional x-ray dark-field imaging of strongly ordered systems”. In: *Physical Review B* 82.21 (2010), p. 214103.

[8] S. Kaeppler et al. “Improved reconstruction of phase-stepping data for Talbot–Lau x-ray imaging”. In: *Journal of Medical Imaging* 4.3 (2017), p. 034005.

[9] S. Kaeppler et al. “Shading Correction for Grating-based Differential Phase Contrast X-ray Imaging”. In: *IEEE Nuclear Science Symposium and Medical Imaging Conference (NSS/MIC)*. Nov. 2014.

[10] S. Kaeppler et al. “Signal Decomposition for X-ray Dark-field Imaging”. In: *International Conference on Medical Image Computing and Computer-Assisted Intervention (MICCAI)*. Sept. 2014, pp. 170–177.

[11] S. Kaeppler et al. “Talbot-Lau X-ray Phase Contrast for Tiling-based Acquisitions without Reference Scanning”. In: *Medical Physics* 44.5 (2017), pp. 1886–1898.

[12] A. Malecki et al. “X-ray tensor tomography”. In: *Europhysics Letters* 105.3 (Feb. 2014), p. 38002.

[13] T. Michel et al. “On a dark-field signal generated by micrometer-sized calcifications in phase-contrast mammography”. In: *Physics in Medicine & Biology* 58.8 (2013), p. 2713.

[14] A. Olivo and R. Speller. “A coded-aperture technique allowing x-ray phase contrast imaging with conventional sources”. In: *Applied Physics Letters* 91 (7 Aug. 2007), p. 074106.

[15] F. Pfeiffer et al. “Phase Retrieval and Differential Phase-contrast Imaging with Low-brilliance X-ray Sources”. In: *Nature Physics* 2.4 (Apr. 2006), pp. 258–261.

[16] R. Raupach and T. Flohr. “Analytical Evaluation of the Signal and Noise Propagation in X-ray Differential Phase-Contrast Computed Tomography”. In: *Physics in Medicine and Biology* 56.7 (Apr. 2011), pp. 2219–2244.

[17] V. Revol et al. “Laminate fibre structure characterisation by orientation-selective X-ray grating interferometry”. In: *Proceedings of the 5th Conference on Industrial Computed Tomography*. Feb. 2014, pp. 45–51.

[18] V. Revol et al. “Sub-pixel Porosity revealed by X-ray Scatter Dark Field Imaging”. In: *Journal of Applied Physics* 110 (2011), p. 044912.

[19] A. Snigirev et al. “On the Possibilities of X-ray Phase Contrast Microimaging by Coherent High Energy Synchrotron Radiation”. In: *Review of Scientific Instruments* 66.12 (Dec. 1995), pp. 5486–5492. DOI: doi:10.1063/1.1146073.

[20] A. Tapfer et al. “Experimental results from a preclinical X-ray phase-contrast CT scanner”. In: *Proceedings of the National Academy of Sciences* 109.39 (2012), pp. 15691–15696.

[21] H. Wen et al. “Fourier X-ray Scattering Radiography Yields Bone Structural Information”. In: *Radiology* 251.3 (June 2009), pp. 910–918.

[22] S. W. Wilkins et al. “Phase-contrast Imaging using Polychromatic Hard X-rays”. In: *Nature* 384.6607 (Nov. 1996), pp. 335–338. DOI: doi:10.1038/384335a0.

[23] A. Yaroshenko et al. “Pulmonary Emphysema Diagnosis with a Preclinical Small-Animal X-ray Dark-Field Scatter-Contrast Scanner”. In: *Radiology* 269.2 (2013), pp. 427–433.